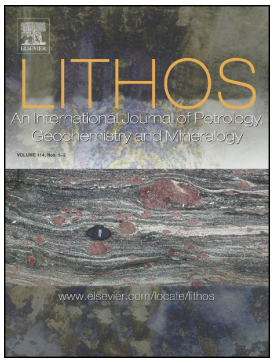

Zircon perspectives on the age and origin of evolved S-type granites from the Cornubian Batholith, Southwest England

W.D. Smith, J.R. Darling, D.S. Bullen, S. Lasalle, I. Pereira, H. Moreira, C.J. Allen, S. Tapster

PII: S0024-4937(19)30125-2
DOI: https://doi.org/10.1016/j.lithos.2019.03.025
Reference: LITHOS 5017

To appear in: *LITHOS*

Received date: 29 October 2018
Accepted date: 20 March 2019

Please cite this article as: W.D. Smith, J.R. Darling, D.S. Bullen, et al., Zircon perspectives on the age and origin of evolved S-type granites from the Cornubian Batholith, Southwest England, LITHOS, https://doi.org/10.1016/j.lithos.2019.03.025

Zircon perspectives on the age and origin of evolved S-type granites from the Cornubian Batholith, southwest England

W.D. Smith[1,2,*] smithwd1@cardiff.ac.uk, J.R. Darling[2], D.S. Bullen[2], S. Lasalle[2], I. Pereira[2], H. Moreira[2], C.J. Allen[2] & S. Tapster[3]

[1]School of Earth & Ocean Sciences, Cardiff University, United Kingdom

[2]School of Earth & Environmental Sciences, University of Portsmouth, United Kingdom

[3]NERC Isotope Geoscience Laboratories, British Geological Survey, Keyworth, United Kingdom

*Corresponding author.

Abstract

Granite stocks across southwest England have played a significant role in the genesis of world-class polymetallic mineralisation. This study presents the first geochemical and geochronological dataset for the composite Crownhill stock, placing it into the newly emerging geochronological framework for the Cornubian Batholith. The Crownhill stock comprises kaolinised two-mica granite in the north and variably-grained biotite granite in the south that encloses pods of tourmaline granite. All granites are peraluminous (A/CNK>1) and the biotite (BG) and tourmaline granites (TG) are related by the replacement of biotite by tourmaline and secondary muscovitization. Integrated LA-ICP-MS and CA-ID-TIMS geochronology indicate two-phase magmatism, where zircon cores yield 288.9 ± 5 Ma and 286.4 ± 5 Ma and rims yield 277.74 ± 0.33 Ma and 278.35 ± 0.35 Ma, for BG and TG respectively. The zircon cores crystallised during initial magmatism, that formed the two-mica and muscovite granites (e.g., Carnmenellis, Bodmin, and Hemerdon) exposed in the north of the Crownhill stock. The zircon rims crystallised from the second phase of magmatism the formed the biotite and tourmaline granites (e.g., Dartmoor and St. Austell). This indicates that zircon crystals were assimilated from older two-mica and muscovite granites and entrained in the second phase of magmatism. Trace element compositions of zircon grains suggest that the rims crystallised from a more evolved magma, where zircon grains hosted in tourmaline granites are broadly more evolved than those from biotite granites. This is likely a result of elevated volatile concentrations delaying zircon fractionation. Trace cassiterite has been observed within interstitial tourmaline in the tourmaline granites, where crystallisation was likely induced by the removal of boron through tourmaline fractionation, coupled with the addition of Sn sourced from the alteration of biotite. The assimilation and over-printing of older granites by second-stage magmatism suggests that the initial phase of magmatism could be more widespread than initially thought and that tourmalinisation may have been responsible for leaching and remobilising Sn from the biotite-rich granites.

Keywords: S-type granite, zircon, U-Pb geochronology, geochemistry, tin-tungsten, Cornubian Batholith

1. Introduction

Peraluminous granites [$Al_2O_3 > (Na_2O+K_2O+CaO)$] occur in orogens across the world (e.g., Sylvester, 1998; Yang et al., 2016), often hosting world-class magmatic and magmatic-hydrothermal ore deposits (Černý et al., 2005; Romer & Kroner, 2016). The Variscan granites of the Cornubian Batholith (Figure 1) were emplaced during early Permian post-collisional extension (Shail & Wilkinson, 1994; Shail & Leveridge, 2009; Simons et al., 2016). Their diachronous emplacement has governed the distribution of tin-tungsten (Sn-W) mineralisation (Jackson et al., 1989; Chesley et al., 1993; Simons et al., 2017). However, recent literature highlights a decoupling between major W- and Sn-forming events, controlled by differing degrees of partial melting of a metasedimentary protolith (Simons et al., 2017). The granites close temporal relationship has made delineating discrete phases of magmatism problematic, augmented by the effects of secondary alteration.

Zircon U-Pb geochronological studies focussed on the crystallisation of the Cornubian Batholith have been largely avoided since S-type granites typically retain a large proportion of inherited zircon grains (Chesley et al., 1993; Neace et al., 2016). In addition, zircon grains hosted in evolved granites typically contain high U (>>100 ppm) concentrations and can therefore, rapidly become metamict (Romer et al., 2007). Thus, the long-standing chronological framework for the granites and associated mineralisation of the region has relied on Rb-Sr whole-rock isochrons (Darbyshire & Shepherd, 1985, 1987) and U-Th-Pb monazite or xenotime studies (Chesley et al., 1993; Chen et al., 1993; Clark et al., 1993). However, the Rb-Sr method is susceptible to resetting during low grade metamorphism (Evans, 1989) and the monazite U-Pb system can be partially reset below 900°C, facilitated by fluid-rock interaction (Williams et al., 2011). New studies have shown that carefully selected magmatic zircon grains are more reliable geochronometers for peraluminous granite emplacement than previously anticipated (Alvarado et al., 2013; Laurent et al., 2017) allowing for new U-Pb and trace element studies to better understand the temporal relationships between granite types and their associated processes.

Some of the least understood granites are located in the eastern Cornubian Batholith. This region encompasses the Dartmoor pluton, which incorporates Lee Moor to the south, adjacent to the Crownhill and Hemerdon stocks, the latter representing a world-class tungsten deposit (Figure 1). These granites were previously believed to be the southern extremity of the Dartmoor pluton (Beer & Scrivener, 1982). Ar-Ar muscovite dating has indicated that the metalliferous Hemerdon granite has a minimum emplacement age of 290 ± 0.4 Ma (Chesley et al. 1993) and therefore, over 10 Myr older than Dartmoor (Figure 2). This study presents the first U-Pb ages and trace element compositions of zircon crystals in the Crownhill stock. We aim to refine the petrogenetic model for the granites exposed in the region, whilst examining the implications that granite magmatism has on Sn-W mineralisation.

2. Regional Setting

Southwest England is primarily composed of Devonian and Carboniferous successions, deposited in an short-lived marginal or successor basin to the Rheic Ocean (e.g., Franke, 2000; Shail & Leveridge, 2009). Rifting in the Early Devonian prompted the formation of a transient passive margin, within which sedimentary successions and rift-related basaltic magmas were emplaced (e.g., Leveridge & Hartley, 2006). The Variscan convergence between Gondwana, Laurussia, and subordinate peri-Gondwana micro-plates was initiated in the Late Devonian (e.g., Shail & Leveridge, 2009; Kroner & Romer, 2013), where continental collision in the Early Carboniferous triggered thin-skinned deformation and regional epizonal-anchizonal metamorphism (Isaac et al., 1982; Warr et al., 1991). During the Early Permian, convergence was succeeded by regional dextral transtension, which reactivated early-Variscan thrusts and associated transfer faults (Shail & Wilkinson, 1994; Shail & Alexander, 1997). The NNE-SSW lithospheric extension led to the emplacement of post-collisional granites and coeval mafic intrusives (Shail & Alexander, 1997; Dupius et al., 2015), alongside contemporaneous aplites and rhyolites (‘elvans’) that locally intrude granites (Simons et al., 2016).

The Cornubian Batholith extends from the Isle of Scilly to Dartmoor and comprises six major plutons and numerous smaller granitic stocks (Figure 1; Dangerfield & Hawkes, 1981). Bott et al. (1958) suggested that the exposed granite plutons are cupolas of a single composite batholith that extends for approximately 250x40 km (Taylor, 2007). However, more recent geochronological investigations (e.g., Chesley et al., 1993; Chen et al., 1993; Tapster et al., 2017) reveal that granite emplacement was progressive over approximately 25 million years.

The batholith displays considerably textural and mineralogical variation (e.g., Dangerfield & Hawkes, 1981; Simons et al., 2016; Figure 1). A crustal origin for the granites has been proposed (e.g., Exley & Stone 1982; Jackson et al., 1989; Chappell & Hine, 2006; Simons et al., 2016, 2017), where a feldspathic metagreywacke is suggested as the protolith (Chappell & Hine, 2006; Simons et al., 2016). The oldest granites (300-288 Ma) represent two-mica (e.g., Bodmin and Carnmenellis) and muscovite granites (e.g., Hemerdon and Carn Brea; Figure 2), whereas the younger granites (284-274 Ma) are composed of composite biotite and tourmaline granites (e.g., Dartmoor, St. Austell and Land's End). Simons et al. (2016) propose a two-stage emplacement model, where the older granites formed through muscovite dehydration melting (731-806°C, >5 kbar), induced by magmatic underplating during ongoing convergence. Increasing temperatures and declining pressures in the lower crust resulted in the melting of more refractory minerals and biotite (770-850°C, 4 kbar), producing the later biotite-dominated granites, which fractionated to produce tourmaline granites. Smaller tourmaline granite pods or orbicules occur in association with biotite granites, likely formed through tourmalinisation (Alderton et al., 1980).

The Crownhill stock is composed of a megacrystic biotite-rich core, bound by a variably-grained biotite granite to the south and a kaolinised two-mica granite to the north (Knox & Jackson, 1990; Figure 1). This is the only stock that comprises granites deriving from both inferred phases of magmatism. Pods of tourmaline granite occur in the biotitic granites of Crownhill and Lee Moor. The advanced weathering of the stock negates a significant geochemical study to resolve its petrogenesis,

however, accessory phase geochronology and geochemistry could provide evidence for two-phase magmatism and help elucidate the petrogenetic relationship between the two.

3. Sampling & Analytical Methods

The granites at Crownhill and Lee Moor (Lee Moor pit) are variably kaolinised, and sampling targeted the least weathered outcrops for geochemical and geochronological analysis. An additional biotite granite sample was collected Blackenstone Quarry in northeast Dartmoor (Figure 1). Polished thin sections were produced at the University of Portsmouth (UoP) for petrological analysis and samples were crushed using standard jaw-crushing and disc-mill techniques. A subsample was powdered for geochemical analysis by XRF, and the remainder was sieved to extract the 50-355 µm fraction from which zircon grains were separated using standard density and magnetic methods at UoP and the University of Bristol. Approximately 200 zircon grains were hand-picked, mounted in epoxy resin, and polished to half-height. Zircon grains were imaged via secondary and backscattered electron techniques to identify compositional domains and mineral defects using a Zeiss EVO MA10 LaB6 scanning electron microscope at UoP. Inclusions were identified using energy dispersive spectroscopy (Oxford Instruments with Aztec Software). Cathodoluminescence (CL) imaging was attempted, but a very low CL response was detected from these grains, which is attributed to their relatively high U contents (MacRae et al., 2014).

The powdered sample for XRF analysis was mixed at a 10:1 ratio with a lithium-metatetraborate flux to produce a homogeneous fusion bead for major element analysis. Pressed powder pellets were used for trace element analysis. A WD Rigaku Primus II XRF was used for measuring major and trace elements and was quantitatively analysed against matrix-matched standards from USGS (JG-1a, JG-3 and JR1). Elements were measured within 5% of their reference values, where MgO and TiO_2 measured within 20% for JR-1 and JG-3, respectively. Additional trace elements (including REEs) were measured in fragments of the fusion beads by laser ablation inductively-coupled plasma mass spectrometry (LA-ICP-MS) using a New Wave UP-213 Nd-YAG 213

nm ablation system, coupled to an Agilent 7500cs Q-ICP-MS. Over two analytical sessions, the machines were optimized using NIST-612 and analyses were standardized to JR1, JG-1a, JG3 and NIST-614 were run as secondary standards to monitor accuracy and precision (Imai et al., 1995). Elements fall within 10% of their published values, whereas Zn, La, EU, Tb, Hf and Ta fall within 20%. Data were reduced using SILLS (Guillong et al., 2008; see Electronic Appendix 1 and 2).

U-Pb geochronological analysis of zircon was conducted using an ASI RESOlution Excimer 193 nm excimer ablation system, coupled to an Analytik Jena Plasma Quant MS, followed by the approach detailed by Moreira et al. (2018). Zircon grains were ablated using 10-15 µm spots (4.5 Jcm^2, 2 Hz) over four analytical sessions. NIST-612 was used to optimise each analytical session, where acceptable tuning criteria included <0.2% oxide production (ThO^+/Th^+ and UO^+/U^+) and $^{232}Th/^{238}U$=1. Plešovice was used as the primary standard to correct for instrumental mass bias, using the reference values in Sláma et al. (2008). Temora 2 (Black et al., 2004), BB9 (Santos et al., 2017) and GJ-1 (Jackson et al., 2004) were analysed as secondary standards, all of which within error of their published values (see Electronic Appendix 3). Monazite U-Th-Pb geochronology used the same instrumentation and were ablated using 5 µm diameter spots (2 Jcm^2, 1`Hz). Results were calibrated against primary standard Itambé over one analytical session (Gonçalves et al., 2016), and FC-1 was analysed as a secondary standard (Horstwood et al., 2003).

All intercept ages in Tera-Wasserburg regressions are anchored to a $^{207}Pb/^{206}Pb$ value of 0.85 (± 0.05) after the Stacey & Kramers (1975) model. Data were reduced in Iolite 3.4 and laser-induced elemental fractionation was corrected using an exponential regression. No common Pb correction was applied (see Electronic Appendix 3).

Concordant zircon grains utilised for LA-ICP-MS were removed from the epoxy mounts and fragmented to remove the tips from the zircon grains, ahead of chemical abrasion isotope dilution thermal ionization mass spectrometry (CA-ID-TIMS). Zircon tips are used instead of whole zircon to bias results towards emplacement ages and not inherited or antecrystic ages. The chemical abrasion

process was based on that of Mattinson (2005) varying leaching times between 8-12 hours based on the size of the zircon fragment analysed. Ion exchange chemistry and subsequent isotopic analysis were carried out at NIGL, British Geological Survey using the ET535 tracer, with isotopic ratios measured using a Thermo-Triton thermal ionisation mass spectrometer. Analytical procedure followed that of Tapster et al. (2016) and was corrected for ^{230}Th disequilibrium using an assumed host Th/U composition of 1.43 (Simons et al., 2017). Uncorrected ages are reported in Electronic Appendix 3.

Zircon trace element analysis used the same instrumentation as LA-ICP-MS geochronology, normalized to NIST-612. Thirty μm spots were ablated on select zircon grains adjacent to previous ablation sites, measuring ^{29}Si, ^{31}P, ^{39}K, ^{42}Ca, ^{45}Sc, ^{49}Ti, ^{51}V, ^{55}Mn, ^{89}Y, ^{91}Zr, ^{93}Nb, ^{118}Sn, ^{122}Sb, ^{133}Cs, ^{139}La, ^{140}Ce, ^{141}Pr, ^{146}Nd, ^{147}Sm, ^{153}Eu, ^{157}Gd, ^{159}Tb, ^{163}Dy, ^{165}Ho, ^{167}Er, ^{169}Tm, ^{173}Yb, ^{175}Lu, ^{178}Hf, ^{182}W, ^{208}Pb, ^{209}Bi, ^{232}Th and ^{238}U (see Electronic Appendix 1). Analysis was internally standardized to stoichiometric SiO_2 concentrations (15.3 Si). NIST-610 (using reported concentrations from Pearce et al., 1997), and 91500 (Wiedenbeck et al., 1995) and GJ-1 were used as secondary standards. Most elements were within 10% of their reference composition and Gd, Tb and U are within 20% (see Electronic Appendix 4).

4. Petrology and Geochemistry

4.1 Major and accessory mineralogy

All granites are porphyritic, with phenocrysts of quartz (8-25 mm) and perthitic orthoclase (10-40 mm) within a fine-grained groundmass of plagioclase, tourmaline, and mica (Table 1). The granites of Crownhill can be divided into three types: (i) biotite (BG), (ii) tourmaline (TG) and (iii) two-mica granites. Each has been subjected to variable degrees of kaolinization and no fresh outcrops of the two-mica granite were located. The granites of Lee Moor are similar to the Crownhill TG, although with greater quartz and muscovite. The BG collected from Blackenstone Quarry is analogous to those collected from Crownhill, with less modal muscovite.

The BGs form a continuum of decreasing plagioclase content from Blackenstone to Crownhill, while orthoclase and quartz (CIPW normative) contents systematically increase (Figure 3a-b). The Crownhill TGs plot within the alkali feldspar granite field, on a QAP diagram whereas the Lee Moor TGs straddle the boundary between quartz-rich and alkali feldspar granite. Minor tourmaline veinlets are seen traversing through BG outcrops, yet no interstitial groundmass tourmaline has been observed. TGs host significant proportions of interstitial tourmaline (Figure 3c). Tourmaline also exists as isolated, euhedral crystals within the TGs with sector zoning (Figure 3d), sometimes with dark blue rims (e.g., Drivenes et al., 2015). Accessory cassiterite (SnO_2) occurs exclusively within TGs as distinct clusters which are spatially associated with interstitial tourmaline (Figure 3e).

4.2 Zircon characteristics

Euhedral zircon grains in the groundmass of all granite types, mostly range from 50 to 300 µm in length. They are found at the boundaries between crystal faces, as well as within fractures in phenocrysts and cleavage planes of micas (Figure 3f). Electron microscopy reveals consistent complex zoning, and the cores of the Crownhill BG and TG zircon grains preserve remnants of oscillatory zoning that have been variably resorbed and fractured (Figure 3g). These zircon grains also have oscillatory-zoned rims that are up to 30 µm in thickness. A few zircon grains possess an encasing metamict crust that is restricted to <20 µm in thickness (Figure 3h). All zircon cores incorporate apatite inclusions, which are not observed in the rims. The rims preserve a diverse inclusion assemblage of monazite (5-50 µm), xenotime (<10 µm), uraninite, thorite, arsenopyrite, cinnabar, galena, chalcopyrite, and wolframite.

4.3 Whole-rock major and trace elements

All samples are peraluminous, with >70 wt.% SiO_2, which generally increases from BG to TG (see Supplementary Table 1). Al_2O_3 exceeds 16 wt.% in the granites from Lee Moor. Conversely, Na_2O, MgO, TiO_2, Fe_2O_3, P_2O_5 and CaO mostly decrease from BG to the muscovite-bearing granites (Figure 4a). A possible geochemical continuum exists between the BGs and TGs from Crownhill, whereas no

clear trends exist in the Lee Moor samples. All samples display similar major element chemistry to previous studies (e.g., Charoy, 1986; Chappell & Hine, 2006; Simons et al., 2016). Blackenstone BG represent the least evolved of the studied granites, with the lowest SiO_2, Al_2O_3 and LOI as well as the highest MgO, FeO, TiO_2 and CaO); this geochemical signature is similar to that reported by Stone (1992; Figure 4b). As Figure 4 shows the BG at Crownhill has slightly more evolved compositions than the Blackenstone BG, with higher SiO_2, K_2O and lower incompatible elements. Biotite granites consistently plot above the zirconium saturation threshold for peraluminous granites at 750°C (>100 ppm) of Watson & Harrison (1983), indicating that saturation concentrations are greater in the BGs (Figure 4c).

Tourmaline granites from both Crownhill and Lee Moor consistently represent the most evolved samples with the highest abundances of Al_2O_3, K_2O and Rb, due to an increase in muscovite (Figure 4d). All BGs have broadly similar Zr concentrations and variable Nb concentrations. TiO_2 against Nb/Ta depicts a curvilinear trend, where Nb/Ta ratios increase from TGs towards Blackenstone BG, which is the least differentiated sample.

All samples are LREE-enriched up to 100x chondrite values, with low Gd/Yb ratios and pronounced negative Eu anomalies (Figure 4g-h), similar to those obtained from other studies (Chappell & Hine, 2006; Simons et al., 2016). Crownhill BG show identical REE trends to the Blackstone BG, which comprises the largest ΣREE contents, the shallowest Eu anomaly (0.54 ± 0.10) and lowest Gd/Yb_{CN} ratio (1.28). Crownhill BGs display an overall, more evolved trend, with more pronounced Eu anomalies (0.36 ± 0.10). Crownhill TG possesses a similar geochemical trend to BG, despite large LREE variability ascribed to the combined effects of tourmalinization and argillic alteration (e.g., Alderton et al., 1980). The HREE trends are almost identical, yet with greater scatter (Gd/Yb_{CN} ranging from 1.29 to 2.83). Lee Moor TGs possess the lowest ΣREE contents (see Electronic Appendix 3).

5. Integrated zircon analyses

5.1 LA-ICP-MS U-Pb geochronology

A total of seventy-seven zircon U-Pb measurements were made by LA-ICP-MS of which, thirty-three targeted resorbed zircon cores and forty-four targeted oscillatory-zoned rims from both the BG and TG. All ages are reported in Supplementary Table 2 and further information provided in Electronic Appendix 3.

From eighteen analyses, nine concordant analyses were obtained from resorbed zircon cores from the BG, yielding a weighted average $^{238}U/^{206}Pb$ age of 289 ± 5 Ma (2σ; Figure 5a-b). Nine discordant analyses were omitted due to the ablation of compromised sectors of zircon grains, identified during post-ablation back-scattered electron observational study (i.e., rim-core mixing, fracturing, and inclusions). Oscillatory-zoned rims were typically thin (< 30 µm) and zircon grains with rims exceeding the diameter of the ablation pit (10-15 µm) were selected for further analysis. From twenty-eight analyses, nine concordant analyses were obtained from zircon rims of BG, yielding a weighted average $^{238}U/^{206}Pb$ age of 276 ± 6 Ma. Nineteen analyses were omitted due to recent Pb-loss and the ablation of compromised sectors of zircon grains, including metamictization.

The same methodology was performed on zircon grains from TG. From fifteen analyses, eleven concordant analyses yielded a weighted average age within uncertainty of BG zircon cores of 286 ± 5 Ma (Figure 5a-c). For oscillatory-zoned rims, eight concordant analyses were obtained from sixteen analyses, yielding a weighted average age of 277 ± 5 Ma. Uranium concentrations are variable between the resorbed cores and the oscillatory-zoned rims of both suites, reaching up to 6,470 ppm in the cores and 8,170 ppm in the rims. Thorium/U values of zircon cores ranges from 0.03 to 0.81, whereas rims range from 0.02 to 0.03, with two anomalous values of 0.72 and 0.80.

Homogeneous monazite inclusions (5-40 µm) embedded within zircon rims were ablated in an attempt to further constrain the inferred two phases of magmatism. Only four concordant analyses were obtained from monazite inclusions in zircon from BGs (see Supplementary Table 3). Acquired dates spanned ages from both zircon cores and rims at 280.0 ± 11 Ma (Figure 6).

5.2 CA-ID-TIMS U-Pb geochronology

The full dataset is reported in Electronic Appendix 3, with the data displayed in Supplementary Table 4. Zircon dates obtained from LA-ICP-MS are consistent with geochronological data derived from CA-ID-TIMS analysis of crystal tips from Crownhill BG (n=6) and TG and all uncertainties are presented at 2σ level (n=4; Figure 5d-e). Uncertainties are presented as ± analytical uncertainty/tracer calibration/decay constant. Seven concordant analyses derived from BG zircon grains yielded $^{206}Pb/^{238}U$ ages ranging from 277.58 to 279.27 Ma. Calculated weighted mean ages generate 277.74 ± 0.10/0.15/0.33 Ma (n=4, MSWD=0.65). Model Th/U ratios range from 0.089 to 0.450 and are calculated based on the assumed concordancy between the U-Pb and Th-Pb systems. Four concordant analyses were obtained from TG zircon grains, possessing a $^{206}Pb/^{238}U$ age range of 278.09 to 279.34 Ma. A Devonian age of 383.99 Ma was also obtained from one fragment; however, this was not reproduced from other analyses. The weighted mean age for TG is 278.35 ± 0.14/0.19/0.35 (n=3, MSWD=0.52), excluding the Devonian zircon. Th/U ratios for Permian ages samples are consistent, ranging from 0.12 to 0.25, whereas, the Devonian sample possesses a Th/U ratio of 1.1. Through combining the results from the two methodologies, two ages groups are apparent, where the 290-285 Ma group correlate with ages from two-mica and muscovite granites, such as Hemerdon and Bodmin, whereas the 280-275 Ma group correlates with BGs, such as Dartmoor and St. Austell (Chesley et al., 1993; Chen et al., 1993).

5.3 LA-ICP-MS trace element analysis

Cores from BG (n=22) have variably high U (184 to 4,000 ppm) and Th (77 to 618 ppm) concentrations, possessing Th/U ratios ranging from 0.038 to 0.810. Hafnium concentrations range from 7,440 to 12,080 ppm (Figure 7a). TG cores (n=19) possess similar U values to BG cores, yet Th values do not exceed 352 ppm, and so Th/U ratios display a smaller range from 0.017 to 0.289. Thorium decreases systematically with increasing Hf, grading from cores to rims, with BG rims (n=6) comprising Th/U ratios from 0.014 to 0.111 and Hf concentrations of 10,880 to 13,230 ppm. TG rims

mirror these values, yet with Hf peaking at 16,600 ppm. Scatter exists in the data due to analytical precision and natural variation within a small dataset (see Supplementary Table 5).

Scandium against Th/U (Figure 7b) shows a curvilinear relationship between the granite suites (BG to TG) and their respective cores and rims. Biotite granite cores range from 100 to 462 ppm, which increases to TG cores with values from 141 to 629 ppm. Scandium begins to increase exponentially with decreasing Th/U, with BG rims peaking at 1,210 ppm and TG rims at 1,470 ppm. This pattern is observed in other trivalent elements (Y, Sb, Bi and LREEs) and W, but not Sn, which is depleted in all but a few BG cores. Using the equation derived by Watson et al. (2006), the temperature of zircon crystallisation can be estimated as $(5080/(6.01\text{Log}(Ti_{zrn}))-273)$, based on the isovalent substitution of Si^{4+} cations by Ti^{4+}. Biotite granite zircon cores retain a crystallisation temperature range of 710 to 875°C (analyses with <5 ppm Ti were discounted as they are below detection limit), whereas TG cores range from 712 to 757°C. The calculated temperatures for the rims overlap with their respective cores.

Niobium and Ta values of zircon cores increase from BG to TG, whereas zircon rims possess variable concentrations of each element (Figure 7c). Nb/Ta ratios in BG cores range from 1.27 to 3.50, whereas TG cores peak at 11.24. Rim concentrations mirror those of their core counterpart, indicative of Nb-enrichment in select TG zircon grains. Zircon grains display characteristic REE trends, with LREEs in all analysed zircon domains ranging from 0.05 to 11 times that of chondritic values (Figure 7e-f). Rim ΣREEs are broadly more enriched relative to chondrites than zircon cores; however, have less prominent Ce and Eu anomalies. Biotite granite zircon rims have the lowest Ce/Ce* values at 0.96 to 1.79, with one anomalous value at 4.51, whereas their cores have Ce/Ce* ratios up to 10.26, with two anomalous values at 27 to 30. Tourmaline granite zircon grains mirror this trend yet are broadly more enriched. Europium anomalies for cores average at 0.08 ± 0.05, whereas rims peak at 0.11 and 0.16 for BGs and TGs, respectively. All samples show HREE enrichment ($La/Yb_{CN} < 0.00561$). Gd/Yb_{CN} ratios prove further HREE enrichment between granite suites and their respective zircon domains (Figure

7d). Zircon cores from BGs range from Gd/Yb_{CN} values of 0.054 to 0.229. Those from TG all reside <0.1. Zircon rims from BGs and TGs continue this trend, where TGs form the base at 0.03 (Gd/Yb_{CN}; see Electronic Appendix 4).

6. Discussion

6.1 Age and origin of the Crownhill stock

Although the granites of the Cornubian Batholith are classified as S-type, significant zircon inheritance was not recorded in this study, allowing precise U-Pb zircon dating of even the most evolved granites in the batholith (e.g., Tapster et al., 2017). Negligible zircon inheritance can only be explained by the source rock being devoid of detrital zircon, as if all refractory zircon was consumed at the source, greater whole-rock Zr concentrations would be expected (Watson & Harrison, 1983). LA-ICP-MS and CA-ID-TIMS analyses collected for this study are in broad agreement, where the fragmented zircon tips correlate with the ablated zircon rims from both granite populations. Zircon cores were only analysed by laser ablation due to the fragmenting technique adopted prior to CA-ID-TIMS analysis.

Laser analysis of zircon cores yielded 288.9 ± 5 Ma and 286.4 ± 5 Ma for BGs and TGs, respectively. These dates from the Crownhill stock and Lee Moor broadly correlate with granites at Bodmin Moor (291.4 ± 0.8 Ma; Chesley et al., 1993), Carnmenellis (293.7 ± 0.6 Ma; Chesley et al., 1993) and other two-mica and muscovite granites dated in the batholith (e.g., Carnmenellis and Carn Brea). Zircon rims from BG and TG yield ages of 275.9 ± 2.3 Ma and 277.6 ± 1.7 Ma, respectively, correlating with biotite granites, including those exposed at Dartmoor and Land's End (280 to 275 Ma; Chesley et al., 1993). However, these separate phases are not resolvable using LA-ICP-MS. The CA-ID-TIMS U-Pb geochronological analysis of zircon tip fragments corroborates the notion of a two-phase magmatic model, yielding ages of 277.74 ± 0.33 Ma and 278.35 ± 0.35 Ma for BG and TG, respectively. These ages replicate those produced from LA-ICP-MS analysis, whilst reducing the uncertainty, making these two phases temporally resolvable. U-Pb geochronology of zircon from the

two-mica granite at Crownhill was hampered by the degree of crystal deformation and metamictisation subjected to the crystal.

The zircon cores derive from older two-mica and muscovite granites. These were likely sourced from granites that comprise the Crownhill two-mica and (or) Hemerdon muscovite granites, somewhere along the migration pathway of the second phase of magmatism. Upon entrainment within the BGs, assimilated zircon were resorbed and acted as a nucleation site for the crystallisation of zircon rims, creating the poly-phase architecture observed in the grains at Crownhill (Figure 8a). This further supports the model of two-stage granite magmatism and records the first evidence from the Cornubian Batholith for zircon inheritance between the two inferred granite phases. Crownhill represents one of the only localities in the batholith where two-mica and biotite granites occur adjacent to each other. Therefore, the assimilation of the former by the latter may not be documented elsewhere in the batholith. Moreover, throughout all analyses carried out in this study, TGs produced the same geochemical and geochronological results as BGs, suggesting a common origin.

Whole-rock geochemistry indicates that the granites exposed at Crownhill are more evolved than those that comprise the Dartmoor pluton (higher SiO_2, Al_2O_3, LILEs, HFSEs). Tourmaline granites across the batholith, occur in association with BGs. The formation of these granites is ascribed to the concentration of boron in the apical parts of a magma chamber, eventually forming a hydrous borosilicate phase, co-existing with the silicate magma (Müller et al., 2006). This phase then intrudes the pluton, forming stocks, orbicules or pods of tourmaline-rich granite (Drivenes et al., 2015). The compositional and textural similarity between TGs exposed at Crownhill and elsewhere in the batholith (e.g., St Austell and Land's End), suggests a similar emplacement model.

Trace elements in zircon suggest that the rims crystallised from a more evolved magma (greater Hf, Ta, Y), derived from a second episode of melting of a similar source rock. Zircon grains in tourmaline granites are broadly more evolved than those from BG. The apical parts of the magma

chamber would have heightened concentrations of boron, which would increase the solubility of zircon and REE-phosphate and delay zircon fractionation (Charoy & Noronha, 1996; Breiter et al., 2006). Given sufficient fractionation, boron would eventually partition into the aqueous fluid phase, typically resulting in localised tourmalinisation, such as that observed at Crownhill (Pollard et al., 1987). Phosphorous and F would also concentrate in the fractionated apical portions of the magma chamber and increase the solubility of zircon (e.g., Keppler, 1993). Lithium would behave similarly, but have the opposite effect on zircon solubility (Linnen, 1998). At Crownhill and Lee Moor, Knox & Jackson (1990) report minor interstitial and pseudomorphic topaz and Li-mica within late-stage aplites, spatially associated with tourmaline veins and pods. This indicates that these elements concentrated together, where B partitioned into the co-existing aqueous fluid phase and F and P was retained in the fractionated melt, which was later expelled as aplitic intrusions (Pollard et al., 1987). Moreover, zircon rims sourced from the TG are consistently depleted in P (Supplementary Table 5), perhaps as a result of co-crystallising apatite (London et al., 1988). The delayed fractionation of zircon is tentatively supported by the broadly lower crystallisation temperatures recorded in TG zircon cores, relative to BG.

6.2 Implications for Sn-W mineralisation

Tin-tungsten mineralisation spans the batholith both spatially and temporally. The older granite plutons and stocks are the most prospective for tungsten-dominated deposits (290 Ma; 401 Mt at 0.13% W and 0.02% Sn; Chesley et al., 1993), Cligga Head (280 Ma; 3000 t W; Dines et al., 1956) and now the W-Sn-Cu Redmoor Prospect (284 Ma; 13.3 Mt at 0.16% W and 0.21% Sn; Chesley et al., 1993; New Age Exploration, 2018). Tin mineralisation typically occurs endogenically, in association with biotite and tourmaline granites. The W/Sn ratio remains broadly consistent across the granite types (see Shepherd et al., 1985), despite recent studies suggesting a temporal decoupling of these elements (Simons et al., 2017; Tapster et al., 2017). Wolframite is noted as the earliest mineralising phase in most paragenetic models in the Cornubian Batholith (Jackson et al., 1989). This suggests that

W was predominantly liberated from the source during the first phase of granite magmatism, whereas, Sn was sequestered in a more refractory host (Romer & Kroner, 2016; Simons et al., 2017). Simons et al. (2017) propose that W is compatible within the muscovite lattice, capable of being liberated during dehydration melting at moderate temperatures and pressure (731-806°C, >5 kbar). Tin however, is concentrated in biotite, together with more refractory minerals, through the isomorphic replacement of Ti^{4+} ($D_{0\text{-}2.32}$; Lehmann, 1982; Williamson et al., 2010), meaning it requires greater temperatures (>1000°C) to extract Sn from the source (Romer & Kroner, 2016).

Cassiterite mineralisation is closely associated tourmaline (Williamson et al., 2010 and this study) and fluorine (Chesley et al., 1993) across the Cornubian Batholith. At Crownhill, cassiterite is associated with tourmaline that display blue overgrowths, a texture ascribed to the crystallisation of a late aqueous fluid (Müller et al., 2005; Drivenes et al., 2015). The pseudomorphic replacement of biotite by tourmaline may have elevated the Sn^{4+} concentration of the borosilicate fluid, increasing the likelihood of cassiterite crystallisation, potentially catalysed by the addition of oxidising meteoric fluids and/or formation waters (Shepherd et al., 1985; Walshe et al., 1996; Duchoslav et al., 2017). It has been experimentally determined that tourmaline replacing biotite would not liberate Sn to the fluid (Hosking, 1964; Alderton & Moore, 1981). However in reduced saline fluids, Sn is more incompatible with tourmaline (<<1,000 ppm; Esmaeily et al., 2005; Williamson et al., 2010). Fluid inclusion work at Dartmoor (Rankin & Alderton, 1983; Alderton et al., 1992), suggests that the Dartmoor BGs were in equilibrium with high-saline fluid (30-50 wt.% NaCl eq.), which would have been capable of liberating Sn from biotite.

6.3 Comparison with Variscan Granites

Monazite and xenotime geochronometers have been used to date the emplacement of peraluminous granites, such as the Central Iberian Zone (CIZ; Valle Aguado et al., 2005), Bohemian Massif (Kusiak et al., 2014) and the French Massif Central (FMC; Laurent et al., 2017). Zircon cores have been often excluded due to metamictisation and inferred crustal inheritance. Zircon textures observed in the

composite Crownhill stock (Figure 8) are similar to those of the FMC (Laurent et al., 2017) and the CIZ (Pereira et al., 2018), where zircon crystals possess resorbed xenocrystic cores derived from the granite protolith, overgrown by oscillatory-zoned rims that crystallised directly from the magma. Post-collisional granite plutonism in the CIZ (310-295 Ma) is also composed of two major magmatic pulses separated by a 5 Ma magmatic hiatus, ascribed to a delayed travel time of the thermal anomaly responsible for partial melting (Gutiérrez-Alonso et al., 2011; Teixeira et al., 2012). Díaz-Alvarado et al. (2016) supports this model by dating poly-phase zircon crystals from the CIZ. These zircon crystals are interpreted to comprise a resorbed antecrystic core derived from the earlier phase of granite magmatism, overgrown by a zircon rim 5 Ma younger within the later phase.

Incompatible fluxing elements (e.g., B, F, P) concentrate in the residual magma during fractional crystallisation (Černý et al., 2005). From this, zircon solubility increases, which delays zircon fractionation and results in a more evolved (greater Hf, Ta and Y) final composition (i.e., the Podlesí granite, Czech Republic, Breiter et al., 2006; Breiter et al., 2016). Cassiterite often crystallises in association with tourmaline derived from exsolved magmatic fluids in highly evolved granites, sometimes together with topaz and Li-mica (Erzgebirge, Štemprok & Blecha, 2015; Western Carpathian granites, Broska & Kubiš, 2018; CIZ, Roda-Robles et al., 2018). This is observed in the Cornubian Batholith (this study and Duchoslav et al., 2017), where cassiterite precipitation is predominantly governed by the redox state of the host fluid. Biotite can readily host Sn^{4+} (Romer & Kroner, 2016; Simons et al., 2017), where Chen et al. (2013) proposes that chloritization of biotite can leach Sn to form cassiterite, however, it is unclear whether tourmalinization can have the same effect. The isovolumetric replacement of biotite by tourmaline is also noted in the Penamacor-Monsato pluton of the CIZ (Da Costa et al., 2014), yet no cassiterite is observed

7. Conclusions

The composite Crownhill stock represents the only stock in the Cornubian Batholith that is composed of two-mica, biotite, and tourmaline granite. Both LA-ICP-MS and CA-ID-TIMS U-Pb geochronology of

poly-phase zircon grains liberated from the biotite and tourmaline granites of Crownhill and Lee Moor support a two-phase magmatic model. Zircon cores yield an age range of 290-288 Ma consistent with older granite plutons (e.g., Bodmin and Carnmenellis), whereas, the corresponding rims yield ages of 278-276 Ma that correlate with younger plutons (e.g., Dartmoor and Land's End). From these ages, we propose that zircon cores crystallised from the initial phase of granite magmatism, to then be assimilated and incorporated into the second phase, which was responsible for crystallising the rims. Trace element data from zircon cores and rims indicate that the rims crystallised from a more evolved magma, where those sampled from tourmaline granites are broadly more evolved that those from biotite granites. This suggests that zircon fractionation was delayed in the tourmaline granites, likely as a result of the increased solubility of zirconium in a volatile-rich portion of a magma chamber. The interaction of borosilicate fluids with antecedent biotite granites could perhaps have triggered the pseudomorphic replacement of biotite by tourmaline. This process could be responsible for liberating Sn from the biotite and henceforth, facilitating the precipitation of cassiterite.

Acknowledgements

This work was supported by the Society of Economic Geologists Hugh E. McKinstry Grant with further support from the Mineralogical Society of Great Britain and Ireland research bursary. W.D.S acknowledges the University of Portsmouth Postgraduate Scholarship Scheme. J.R.D acknowledges a Higher Education Innovation Fund grant and Researcher Development Fund grant from the University of Portsmouth. The authors thank Wolf Minerals and Sibelco for providing samples, supplementary data and site access. Academic and technical staff at UoP are acknowledged for advice and help during sample preparation and analytical procedures, particularly Joe Dunlop and Mike Fowler. Bruno Dhuime is thanked for his assistance during mineral separation at the University of Bristol. Richard Scrivener is thanked for his guidance and advice throughout the project. Andrew Kerr, Beth Simons,

and one anonymous reviewer are thanked for their constructive comments that greatly improved the manuscript. Nelson Eby and Michael Roden are thanked for their editorial handling.

References

Aguado, B. V., Azevedo, M. R., Schaltegger, U., Catalán, J. M., & Nolan, J. (2005). U–Pb zircon and monazite geochronology of Variscan magmatism related to syn-convergence extension in Central Northern Portugal. Lithos, 82(1-2), pp. 169-184.

Alderton, D. H., Rankin, A. H., & Thompson, M. (1992). Fluid inclusion chemistry as a guide to tin mineralization in the Dartmoor granite, south-west England. Journal of Geochemical Exploration, 46(2), pp. 163-185.

Alderton, D. H. M., & Moore, F. (1981). New determinations of tin and tungsten in granites from south-west England. Mineralogical Magazine, 44(335), pp. 354-356.

Alderton, D. H. M., Pearce, J. A., & Potts, P. J. (1980). Rare earth element mobility during granite alteration: evidence from southwest England. Earth and Planetary Science Letters, 49(1), pp. 149-165.

Beer, K., & Scrivener, R. (1982). Metalliferous mineralisation. In L. D. Durrance E.M. (Ed.). The geology of Devon (p. 117-147). University of Exeter.

Black, L. P., Kamo, S. L., Allen, C. M., Davis, D. W., Aleinikoff, J.N, J. N., Valley, J. W., Mundil, R., Campbell, I.H., Korsch, R.J., Williams, I.S. & Foudoulis, C. (2004). Improved $^{206}Pb/^{238}U$ microprobe geochronology by the monitoring of a trace-element-related matrix effect; SHRIMP, ID-TIMS, ELA-ICP-MS and oxygen isotope documentation for a series of zircon standards. Chemical Geology, 205(1-2), pp. 115-140.

Bott, M. H. P., Day, A. A., & Masson-Smith, D. (1958). The geological interpretation of gravity and magnetic surveys in Devon and Cornwall. Phil. Trans. R. Soc. Lond. A, 251(992), pp. 161-191.

Boynton, W. V. (1985). Chapter 3. Cosmochemistry of the rare earth elements: Meteorite studies. In P. Henderson, Rare Earth Element Geochemistry, pp. 115-1522.

Breiter, K., Müller, A., Shail, R., & Simons, B. (2016). Composition of zircon grains from the Cornubian Batholith of SW England and comparison with zircon grains from other European Variscan rare-metal granites. Mineralogical Magazine, 80(7), pp. 1273-1289.

Breiter, K., Förster, H. J., & Škoda, R. (2006). Extreme P-, Bi-, Nb-, Sc-, U-and F-rich zircon from fractionated perphosphorous granites: The peraluminous Podlesí granite system, Czech Republic. Lithos, 88(1-4), pp. 15-34.

Broska, I., & Kubiš, M. (2018). Accessory minerals and evolution of tin-bearing S-type granites in the western segment of the Gemeric Unit (Western Carpathians). Geologica Carpathica, 69(5), pp. 483-497.

Chadwick, R. A., & Evans, D. J. (1995). The timing and direction of Permo-Triassic extension in southern Britain. Geological Society Special Publication, 91, pp. 161-192.

Chappell, B. W., & Hine, R. (2006). The Cornubian Batholith: An example of magmatic fractionation on a Crustal Scale. Resource Geology, 56(3), pp. 203-244.

Charoy, B. (1986). The Genesis of the Cornubian Batholith (South-West England): the example of the Carnmenellis Pluton. Journal of Petrology, 27(3), pp. 571-604.

Charoy, B., Noronha, F. (1996); Multistage Growth of a Rare-Element, Volatile-Rich Microgranite at Argemela (Portugal), Journal of Petrology, 37(1), pp. 73–94.

Chen, Y., Clark, A. H., Farrar, E., Wasteneys, H. A., Hodges on, M. J., & Bromley, A. V. (1993). Diachronous and independent histories of plutonism and mineralisation in the Cornubian Batholith, southwest England. Journal of the Geological Society of London, 150, pp. 1183-1191.

Chen, J., Wang, R., Zhu, J., Lu, J., & Ma, D. (2013). Multiple-aged granitoids and related tungsten-tin mineralization in the Nanling Range, South China. Science China Earth Sciences, 56(12), pp. 2045-2055.

Chesley, J. T., Halliday, A. N., See, L. W., Meager, K., Shepherd, T. J., & Scrivener, R. C. (1993). Thermochronology of the Cornubian Batholith in southwest England: Implications for pluton emplacement and protracted hydrothermal mineralisation. Geochimica et Cosmochimica Acta, 57, pp. 1817-1835.

Clark, A. H., Chen, Y., Farrar, E., Wasteneys, H. A., Stimac, J. A., & Hodgson, M. J. (1993). The Cornubian Sn-Cu (-As, W) Metallogenic Province: Product of a 30My History of discrete and concomitant anatectic, intrusive and hydrothermal events. Proceedings of the Ussher Society, 8, pp. 112-116.

Černý, P., Blevin, P.L., Cuney, M., London, D (2005). Granite-related ore deposits. Society of Economic Geologists, 100th Anniversary, pp. 337-370.

Da Costa, I. R., Mourão, C., Récio, C., Guimarães, F., Antunes, I. M., Ramos, J. F., ... & Milton, J. A. (2014). Tourmaline occurrences within the Penamacor-Monsanto granitic pluton and host-rocks (Central Portugal): genetic implications of crystal-chemical and isotopic features. Contributions to Mineralogy and Petrology, 167(4), pp. 993.

Dangerfield, J., & Hawkes, J. R. (1981). The Variscan granites of south-west England: additional information. Proceedings of the Ussher Society, 5, pp. 116-120.

Darbyshire, D. P., & Shepherd, T. J. (1985). Chronology of granite magmatism and associated mineralisation, SW England. Journal of the Geological Society of London, 142, pp. 1159-1177

Darbyshire, D.P.F., Shepherd, T.J. (1987). Chronology of magmatism in south-west England: the minor intrusions. Proceedings of the Ussher Society, 6, pp. 431-438.

Dines, H.G., 1956. The metalliferous mining region of south-west England. Volume 1. HM Stationery Office.

Díaz-Alvarado, J., Fernández, C., Chichorro, M., Castro, A., & Pereira, M. F. (2016). Tracing the Cambro-Ordovician ferrosilicic to calc-alkaline magmatic association in Iberia by in situ U–Pb SHRIMP

zircon geochronology (Gredos massif, Spanish Central System batholith). Tectonophysics, 681, pp. 95-110.

Drivenes, K., Larsen, R. B., Müller, A., Sørensen, B. E., Wiedenbeck, M., & Raanes, M. P. (2015). Late-magmatic immiscibility during batholith formation: assessment of B isotopes and trace elements in tourmaline from the Land's End granite, SW England. Contributions to Mineralogy and Petrology, 169(6), pp. 56.

Duchoslav, M., Marks, M. A. W., Drost, K., McCammon, C., Marschall, H. R., Wenzel, T., & Markl, G. (2017). Changes in tourmaline composition during magmatic and hydrothermal processes leading to tin-ore deposition: The Cornubian Batholith, SW England. Ore Geology Reviews, 83, pp. 215-234.

Dupuis, N. E., Braid, J. A., Murphy, J. B., Shail, R. K., Archibald, D. A., & Nance, R. D. (2015). 40Ar/39Ar phlogopite geochronology of lamprophyre dykes in Cornwall, UK: new age constraints on Early Permian post-collisional magmatism in the Rhenohercynian Zone, SW England. Journal of the Geological Society, pp. 2014-151.

Esmaeily, D., Nédélec, A., Valizadeh, M. V., Moore, F., & Cotten, J. (2005). Petrology of the Jurassic Shah-Kuh granite (eastern Iran), with reference to tin mineralisation. Journal of Asian Earth Sciences, 25(6), 961-980.

Evans, J.A., 1989. Short Paper: A note on Rb-Sr whole-rock ages from cleaved mudrocks in the Welsh Basin. Journal of the Geological Society, 146(6), pp.901-904.

Exley, C. S., & Stone, M. (1982). Hercynian intrusive rocks. In D. S. Sutherland, Igneous Rocks of the British Isles, pp. 287-320.

Franke, W., Haak, V., Oncken, O., & Tanner, D. (2000). Orogenic processes: quantification and modelling in the Variscan belt. Geological Society, London, Special Publications, 179(1), pp. 1-3.

Gonçalves, G.O., Lana, C., Scholz, R., Buick, I.S., Gerdes, A., Kamo, S.L., Corfu, F., Marinho, M.M., Chaves, A.O., Valeriano, C. and Nalini Jr, H.A., 2016. An assessment of monazite from the Itambé

pegmatite district for use as U–Pb isotope reference material for microanalysis and implications for the origin of the “Moacyr” monazite. Chemical Geology, 424, pp. 30-50.

Guillong, M., Meier, D. L., Allan, M. M., Heinrich, C. A., & Yardley, B. W. (2008). SILLS: a MATLAB-based program for the reduction of laser ablation ICP-MS data of homogeneous materials and inclusions. In P. Sylvester, Laser Ablation ICP-MS in the Earth Sciences: Current Practices and Outstanding Issues, 40, pp. 328-333. Mineral Association of Canada: Short Course Series.

Gutiérrez-Alonso, G., Fernández-Suárez, J., Jeffries, T.E., Johnston, S.T., Pastor-Galán, D., Murphy, J.B., Franco, M.P, and Gonzalo, J.C (2011). Diachronous post-orogenic magmatism within a developing orocline in Iberia, European Variscides. Tectonics, 30(5), pp. 1-17.

Horstwood, M. S., Foster, G. L., Parrish, R. R., Noble, S. R., & Nowell, G. M. (2003). Common-Pb corrected in situ U–Pb accessory mineral geochronology by LA-MC-ICP-MS. Journal of Analytical Atomic Spectrometry, 18(8), pp. 837-846.

Hosking, K.F.G. (1964). Permo-Carboniferous and later mineralisation of Cornwall and south-west Devon in Hosking & Shrimpton (eds). Present views of some aspects of the geology of Cornwall and Devon. Pp. 201-245.

Imai, N., Terashima, S., Itoh, S., & Ando, A. (1995). 1994 compilation of analytical data for minor and trace elements in seventeen GSJ geochemical reference samples, "Igneous rock series". Geostandards Newsletter, 19, pp. 135-213.

Isaac, K. P., Turner, P. J., & Stewart, I. J. (1982). The evolution of the Hercynides of central SW England. Journal of the Geological Society of London, 139, pp. 521-521.

Jackson, N. J., Willis-Richards, J., Manning, D. A., & Sams, M. S. (1989). Evolution of the Cornubian Ore Field, Southwest England: Part II. Mineral Deposits and Ore-Forming Processes. Economic Geology, 84, pp. 1101-1133.

Jackson, S. E., Pearson, N. J., Griffin, W. L., & Belousova, E. A. (2004). The application of laser ablation-inductively coupled plasma-mass spectrometry to in situ U/Pb zircon geochronology. Chemical Geology, 211(1-2), pp. 47-69.

Keppler, H. (1993). Influence of fluorine on the enrichment of high field strength trace elements in granitic rocks. Contributions to Mineralogy and Petrology, 114(4), pp. 479-488.

Knox, D. A., & Jackson, N. J. (1990). Composite granite intrusions of SW Dartmoor, Devon. Proceedings of the Ussher Society, 7, pp. 246-251.

Kroner, U., & Romer, R. L. (2013). Two plates—many subduction zones: the Variscan orogeny reconsidered. Gondwana Research, 24(1), pp. 298-329.

Kusiak, M. A., Williams, I. S., Dunkley, D. J., Konečny, P., Słaby, E., & Martin, H. (2014). Monazite to the rescue: U–Th–Pb dating of the intrusive history of the composite Karkonosze pluton, Bohemian Massif. Chemical Geology, 364, pp. 76-92.

Laurent, O., Couzinié, S., Zeh, A., Vanderhaeghe, O., Moyen, J. F., Villaros, A., ... & Chelle-Michou, C. (2017). Protracted, coeval crust and mantle melting during Variscan late-orogenic evolution: U–Pb dating in the eastern French Massif Central. International Journal of Earth Sciences, 106(2), pp. 421-451.

Lehmann, B. (1982). Metallogeny of tin; magmatic differentiation versus geochemical heritage. Economic Geology, 77(1), pp. 50-59.

Leveridge, B., & Hartley, A. J. (2006). The Variscan Orogeny: the development and deformation of Devonian/Carboniferous basins in SW England and South Wales. In: The geology of England and Wales/edited by PJ Brenchley and PF Rawson. London: Geological Society of London, 2006, pp. 225-255.

Linnen, R. L. (1998). The solubility of Nb-Ta-Zr-Hf-W in granitic melts with Li and Li+ F; constraints for mineralization in rare metal granites and pegmatites. Economic Geology, 93(7), pp. 1013-1025.

London, D., Hervig, R. L., & Morgan, G. B. (1988). Melt-vapor solubilities and elemental partitioning in peraluminous granite-pegmatite systems: experimental results with Macusani glass at 200 MPa. Contributions to Mineralogy and Petrology, 99(3), pp. 360-373.

MacRae, C., Wilson, N., Torpy, A., Pownceby, M., Hanchar, J., Davidson, C., & Hugo, V. (2014). Zircon Metamictisation study by Cathodoluminescence and X-ray Imaging. Microscopy and Microanalysis, 20(S3), pp. 908-909.

Manning, D.A.C., Hill, P.I., Howe, J.H (1996). Primary lithological variation in the kaolinized St. Austell Granite, Cornwall, England. Journal of the Geological Society, 153, pp. 827-838.

Mattinson, J. M. (2005). Zircon U-Pb chemical abrasion ("CA-TIMS") method: Combined annealing and multi-step partial dissolution analysis for improved precision and accuracy of zircon ages. Chemical Geology, 220 (1-2), pp. 46-66.

Moreira, H., Seixas, L., Storey, C., Fowler, M., Lasalle, S., Stevenson, R., & Lana, C. (2018). Evolution of Siderian juvenile crust to Rhyacian high Ba-Sr magmatism in the Mineiro Belt, southern São Francisco Craton. Geoscience Frontiers, 9(4), pp. 977-995.

Müller, A., Seltmann, R., Halls, C., Siebel, W., Dulski, P., Jeffries, T., ... & Kronz, A. (2006). The magmatic evolution of the Land's End pluton, Cornwall, and associated pre-enrichment of metals. Ore Geology Reviews, 28(3), pp. 329-367.

Müller, A., & Halls, C. (2005). Rutile—the tin-tungsten host in the intrusive tourmaline breccia at Wheal Remfry, SW England. In Mineral Deposit Research: Meeting the Global Challenge, pp. 441-444.

Nance, R. D., Gutierrez-Alonso, G., Keppie, J. D., Linnemann, U., Murphy, J. B., Quesada, C., Strachan R.A., Woodcock, N. H. (2010). Evolution of the Rheic Ocean. Gondwana Research, 17, pp. 194-222.

Neace, E. R., Nance, R. D., Murphy, J. B., Lancaster, P. J., & Shail, R. K. (2016). Zircon LA-ICPMS geochronology of the Cornubian Batholith, SW England. Tectonophysics, 681, pp. 332–352.

New Age Exploration, Cornwall Resources Limited & SRK Exploration. (2018). Redmoor 2018 Mineral Resource Update.

Pearce, N. J. G., Perkins, W. T., Westgate, J. A., Gorton, M. P., Jackson, S. E. C., Neal, R., Chenery, S. P. (1997). A compilation of new and published major and trace element data for NIST SRM 610 and NIST SRM 612 glass reference materials, Geostandards Newsletter, 21, pp. 115–144.

Pereira, M. F., Castro, A., Fernández, C., & Rodríguez, C. (2018). Multiple Paleozoic magmatic-orogenic events in the Central Extremadura batholith (Iberian Variscan belt, Spain). Journal of Iberian Geology, pp. 1-25.

Pollard, P. J., Pichavant, M., & Charoy, B. (1987). Contrasting evolution of fluorine-and boron-rich tin systems. Mineralium Deposita, 22(4), pp. 315-321.

Rankin, A.H. & Alderton, D.H.M. (1983). Fluid Inclusion Petrography of SW England Granites and its Potential in Mineral Exploration. Mineral Deposita 18(2), pp. 335-347.

Roda-Robles, E., Villaseca, C., Pesquera, A., Gil-Crespo, P. P., Vieira, R., Lima, A., & Garate-Olave, I. (2018). Petrogenetic relationships between Variscan granitoids and Li-(FP)-rich aplite-pegmatites in the Central Iberian Zone: Geological and geochemical constraints and implications for other regions from the European Variscides. Ore Geology Reviews, 95, pp. 408-430.

Romer, R. L., & Kroner, U. (2016). Phanerozoic tin and tungsten mineralization—tectonic controls on the distribution of enriched protoliths and heat sources for crustal melting. Gondwana Research, 31, pp. 60-95.

Romer, R. L., Thomas, R., Stein, H. J., & Rhede, D. (2007). Dating multiply overprinted Sn-mineralized granites—examples from the Erzgebirge, Germany. Mineralium Deposita, 42(4), pp. 337-359.

Santos, M. M., Lana, C., Scholz, R., Buick, I., Schmitz, M. D., Kamo, S. L., Corfu, F., Tapster, S., Lancaster, P., Storey, C.D., Basei, M.A.S., Tohver, E., Alkmim, A., Nalini, H., Krambrock, K., Fantini, C., Wiedenbeck, M. (2017). A New Appraisal of Sri Lankan BB Zircon as a Reference Material for LA-ICP-

MS U-Pb Geochronology and Lu-Hf Isotope Tracing. Geostandards and Geoanalytical Research, 41(3), pp. 335-358.

Shail, R. K., & Alexander, A. C. (1997). Late Carboniferous to Triassic reactivation of Variscan basement in the western English Channel: evidence from onshore exposures in south Cornwall. Journal of the Geological Society, 154, pp. 163-168.

Shail, R. K., & Wilkinson, J. J. (1994). Late-to Post-Variscan Extensional Tectonics in South Cornwall. Proceedings of the Ussher Society, 8, pp. 262-270.

Shail, R. K., & Leveridge, B. E. (2009). The Rhenohercynian passive margin of SW England: Development, inversion and extensional reactivation. Comptes Rendus Geoscience, 341(2-3), pp. 140-155.

Shepherd, T. J., Miller, M. F., Scrivener, R. C., & Darbyshire, D. P. (1985). Hydrothermal fluid evolution in relation to mineralisation in southwest England with special reference to the Dartmoor-Bodmin area in High heat production (HHP) granites, hydrothermal circulation and ore genesis, 1, pp. 345-364.

Simons, B., Shail, R. K., & Anderson, J. C. (2016). The petrogenesis of the Early Permian Variscan granites of the Cornubian Batholith: Lower plate post-collisional peraluminous magmatism in the Rhenohercynian Zone of SW England. Lithos, 260, pp. 76-94.

Simons, B., Anderson, J. C., Shail, R. K., & Jenner, F. (2017). Fractionation of Li, Be, Ga, Nb, Ta, In, Sn, Sb, W and Bi in the peraluminous Early Permian Variscan granites of the Cornubian Batholith: precursor processes to magmatic-hydrothermal mineralisation. Lithos, 278-281, pp. 491-512.

Sláma, J., Košler, J., Condon, D. J., Crowley, J. L., Gerdes, A., Hanchar, J. M., Whitehouse, M. J. (2009). Plešovice zircon — A new natural reference material for U–Pb and Hf isotopic microanalysis. Chemical Geology, 249, pp. 1-35.

Stacey, J. S., & Kramers, J. D. (1975). Approximation of Terrestrial Lead Isotope Evolution by a 2-Stage Model. Earth and Planetary Science Letters, 26(2), pp. 207-221.

Štemprok, M., & Blecha, V. (2015). Variscan Sn–W–Mo metallogeny in the gravity picture of the Krušné hory/Erzgebirge granite batholith (Central Europe). Ore Geology Reviews, 69, pp. 285-300.

Stone, M. (1992). The Tregonning granite: petrogenesis of Li-mica granites in the Cornubian batholith. Mineralogical Magazine, 56(383), pp. 141-155.

Sylvester, P. J. (1998). Post-collisional strongly peraluminous granites. Lithos, 45, pp. 29-44.

Tapster, S., Condon, D.J., Naden, J., Noble, S.R., Petterson, M.G., Roberts, N.M.W., Saunders, A.D. and Smith, D.J. (2016). Rapid thermal rejuvenation of high-crystallinity magma linked to porphyry copper deposit formation; evidence from the Koloula Porphyry Prospect, Solomon Islands. Earth and Planetary Science Letters, 442, pp.206-217.

Tapster, S., Shail, R. K., McAllister, H., Deady, E., & McFarlane, J. (2017). Understanding the multi-episode formation of the world-class Hemerdon W–Sn deposit in the context of SW England granite evolution. Applied Earth Science.

Taylor, G. K. (2007). Pluton shapes in the Cornubian Batholith: new perspectives from gravity modelling. Journal of the Geological Society, 164(3), pp. 525-528.

Teixeira, R. J. S., Neiva, A. M., Gomes, M. E. P., Corfu, F., Cuesta, A., & Croudace, I. W. (2012). The role of fractional crystallisation in the genesis of early syn-D3, tin-mineralized Variscan two-mica granites from the Carrazeda de Ansiães area, northern Portugal. Lithos, 153, pp. 177-191.

Walshe, J. L., Halley, S. W., Anderson, J. A., & Harrold, B. P. (1996). The interplay of groundwater and magmatic fluids in the formation of the cassiterite-sulfide deposits of western Tasmania. Ore Geology Reviews, 10(3-6), pp. 367-387.

Warr, L. N., Primmer, T. J., & Robinson, D. (1991). Variscan very low-grade metamorphism in southwest England: a diastathermal and thrust-related origin. Journal of Metamorphic Geology, 9(6), pp. 751-764.

Watson, E. B., & Harrison, T. M. (1983). Zircon saturation revisited: temperature and composition effects in a variety of crustal magma types. Earth and Planetary Science Letters, 64(2), pp. 295-304.

Watson, E. B., Wark, D. A., & Thomas, J. B. (2006). Crystallisation thermometers for zircon and rutile. Contributions to Mineralogy and Petrology, 151(4), pp. 413.

Wiedenbeck, M., Allé, P., Corfu, F., Griffin, W. L., Meier, M., Orbeli, F., Spiegel, W. (1995). Three natural zircon standards for U-Th-Pb, Lu-Hf, trace element and REE analyses. Geostandards Newsletter, 19, pp. 1-23.

Williams, M. L., Jercinovic, M. J., Harlov, D. E., Budzyn, B., & Hetherington, C. J. (2011). Resetting monazite ages during fluid-related alteration. Chemical Geology, 283(3-4), pp. 218-225.

Williamson, B. J., Müller, A. and Shail, R. K. (2010) 'Source and partitioning of B and Sn in the Cornubian batholith of southwest England', Ore Geology Reviews. Elsevier B.V., 38(1–2), pp. 1–8.

Yang, H., Zhang, H., Luo, B., Gao, Z., Guo, L., & Xu, W. (2016). Generation of peraluminous granitic magma in a post-collisional setting: a case study from the eastern Qilian orogen, NE Tibetan Plateau. Gondwana Research, 36, pp. 28-45.

Figure Captions

Figure 1. Surface expressions of the Cornubian Batholith in SW England (modified from Dangerfield & Hawkes 1981; Exley & Stone 1982; Simons et al., 2016) with an inset map of the Crownhill area (modified from Knox & Jackson, 1990). *VP, variably porphyritic; HD, Hingston Down; KH, Kit Hill; BB, Belowda Beacon; CD, Castle-an-Dinas; CH, Cligga Head; SA, St. Agnes; CB, Carn Brea; CM, Carn Marth.

Figure 2. Compilation of the previous geochronological studies of granites and associated mineralisation within the Cornubian Batholith. G1 represents the two-mica and muscovite granites and G2 represents biotite and tourmaline granites. [1]Nance et al., (2010); [2]Shail & Alexander (1997); [3]Chadwick & Evans (1995); [4]Neace et al., (2015); [5]Chesley et al., (1993); [6]Chen et al., (1993); [7]Clark et al., (1993); [8]Darbyshire & Shepherd (1987). Fl, Fluorite; SC, South Crofty; WR, Wheal Remfry; GSV, Greisen-sheeted vein.

Figure 3. a. CIPW-normative QAP plot. b. Inclusions within perthitic orthoclase (HP02). c. Interstitial tourmaline amongst qtz and plg (HP06). d. Sub-hedral isolated tourmaline amongst muscovite aggregates (LM01). e. Twinned cassiterite crystals within tourmaline vein (HP05). f. Zircon within quartz phenocryst (HP01). g. Zircon from TG, displaying zoning and a monazite inclusion (HP05). h. Zircon from BG displaying internal zoning and a metamict crust (HP02). Qtz, quartz; Bt, biotite; Or, orthoclase; Plg, plagioclase; Tur, tourmaline; Ms, muscovite; Cst, cassiterite; Zrn, zircon; Mnz, monazite; Ap, apatite.

Figure 4. Whole-rock geochemistry plots, where plots b-e are underlain with granite geochemistry collated from Simons et al. (2016). a. A/NK versus A/CNK diagram. b. MgO versus SiO_2. c. Zr versus TiO_2, overlain with the Zr saturation threshold (Watson & Harrison, 1983). d. Rb versus TiO_2. e. Zr versus Nb with ratios overlain from Manning et al., (1996). f. Nb/Ta versus TiO_2 with magmatic-hydrothermal transition (MHT) index numbers. g-h. Rare earth element spider plots for BG (g) and TG (h), normalised to the chondrite values of Boynton (1985).

Figure 5. a. Back-scatter electron images of ablated zircon grains with their corresponding ages. b. LA-ICP-MS Tera-Wasserburg diagram of BG zircon cores and rims, with regression line fixed at 0.85 after Stacey & Kramers (1975) model, presented ages are weighted averages. c. LA-ICP-MS Tera-Wasserburg diagram of TG zircon cores and rims, with fixed regression line and weighted average ages. d. Concordia plot of BG and TG samples from CA-ID-TIMS analysis. e. CA-ID-TIMS calculated and weighted average ages from BG and TG.

Figure 6. LA-ICP-MS U-Pb monazite geochronology for monazite inclusions within zircon rims. Only monazite inclusions within zircon grains from BGs were capable of being dated, due to their size and homogeneity. The age presented is a mean concordia age of $^{206}Pb/^{238}U$ (2σ).

Figure 7. a-d Th/U against Hf, Sc, Nb/Ta and Gd/Yb. e-f. Chondrite-normalised REE plots (Boynton, 1985), where both granite types display similar trends, with variably positive Ce anomalies and pronounced negative Eu anomalies.

Figure 8. a. The internal morphology of zircon grains used for this study. Monazite inclusions are exclusive to zircon rims. b. $^{238}U/^{206}Pb$ ages (Ma) against Th/U of all geochronological analyses from this study.

Table Captions

Table 1. Petrographic summary of the granite types sampled for this study.

Supplementary Data

Supplementary Figure 1. a. LA-ICP-MS Tera-Wasserburg diagram of BG zircon cores and rims from Blackenstone Quarry, with regression line fixed at 0.85 after Stacey & Kramers (1975) model, presented ages are weighted averages. b. LA-ICP-MS Tera-Wasserburg diagram of BG zircon cores and rims from Lee Moor. c. Results from concordant analysis obtained from CA-ID-TIMS analysis of

Blackenstone BG zircon grains. Here it is presented with calculated and weighted average ages. d. Results from concordant analysis obtained from CA-ID-TIMS analysis of Lee Moor TG.

Supplementary Table 1. Whole-rock geochemistry for samples used for this study.

Supplementary Table 2. LA-ICP-MS U-Pb zircon geochronology dataset for granites at Crownhill.

Supplementary Table 3. LA-ICP-MS U-Pb monazite geochronology dataset for BG at Crownhill.

Supplementary Table 4. CA-ID-TIMS U-Pb zircon geochronology dataset for granites at Crownhill.

Supplementary Table 5. Representative dataset for LA-ICP-MS zircon trace element analysis, including the Ti-in-Zrn thermometer [1] (Watson & Harrison, 1983).

Table 1. Petrographic summary of the granite types sampled for this study.

Granite	Biotite Granite (BG)	Tourmaline Granite (TG)
Grain Size	Predominately medium to coarse grained, up to megacrystic	Fine to medium grained
Texture	Moderately to strongly porphyritic with Or (6-15 mm) and Qtz (2-10 mm) phenocrysts	Weakly porphyritic with Or (ca. 5 mm) and Qtz (1-3 mm) phenocrysts
Grain Dispersal	All minerals dispersed throughout samples	Clusters of interstitial tourmaline and poorly distributed aggregates of muscovite
Major Mineralogy	Qtz, Or, Pl, Bt	Qtz, Or, Pl, Tur, Ms
Minor Mineralogy	Ms, Tur, Zrn, Ap, Mnz, Xtm, Fe-oxide	Bt, Zrn, Ap, Mnz, Xtm, Cst, Fe-oxide
Notes	Two-stage Or phenocryst growth. Minor argillic alteration of Pl.	Aggregates of Ms. Interstitial Tur replacing Bt. Greater degree of argillic alteration of Pl and Or.

Highlights

- The first integrated study of the Crownhill stock in the Cornubian Batholith
- LA-ICP-MS and CA-ID-TIMS U-Pb zircon geochronology reveal bimodal magmatism
- Polyphase zircon develop via the reworking of older granite by younger granite
- Cassiterite precipitation is catalysed by the tourmalinisation of biotite

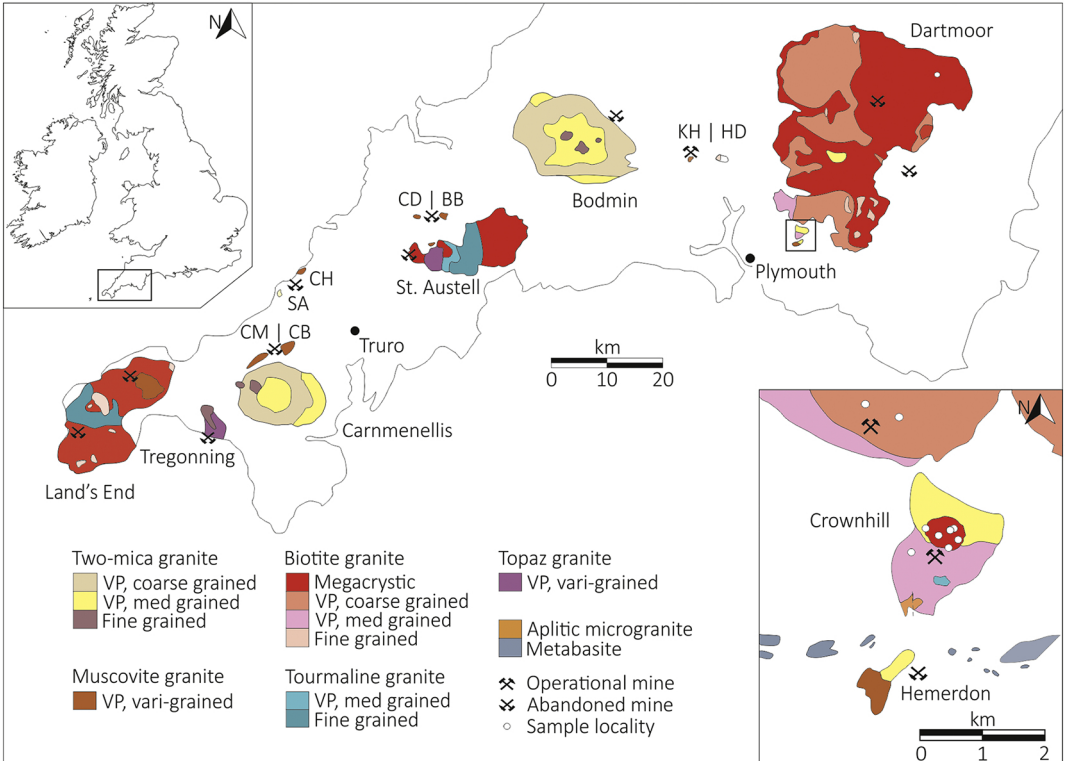
N
Dartmoor
KH | HD
Bodmin
CD | BB
St. Austell
CH
SA
Plymouth
CM | CB
Truro
km
0 10 20
Carnmenellis
Tregonning
Land's End
Two-mica granite
VP, coarse grained
VP, med grained
Fine grained
Biotite granite
Megacrystic
VP, coarse grained
VP, med grained
Fine grained
Topaz granite
VP, vari-grained
Aplitic microgranite
Metabasite
Muscovite granite
VP, vari-grained
Tourmaline granite
VP, med grained
Fine grained
Operational mine
Abandoned mine
Sample locality
N
Crownhill
Hemerdon
km
0 1 2

Figure 1

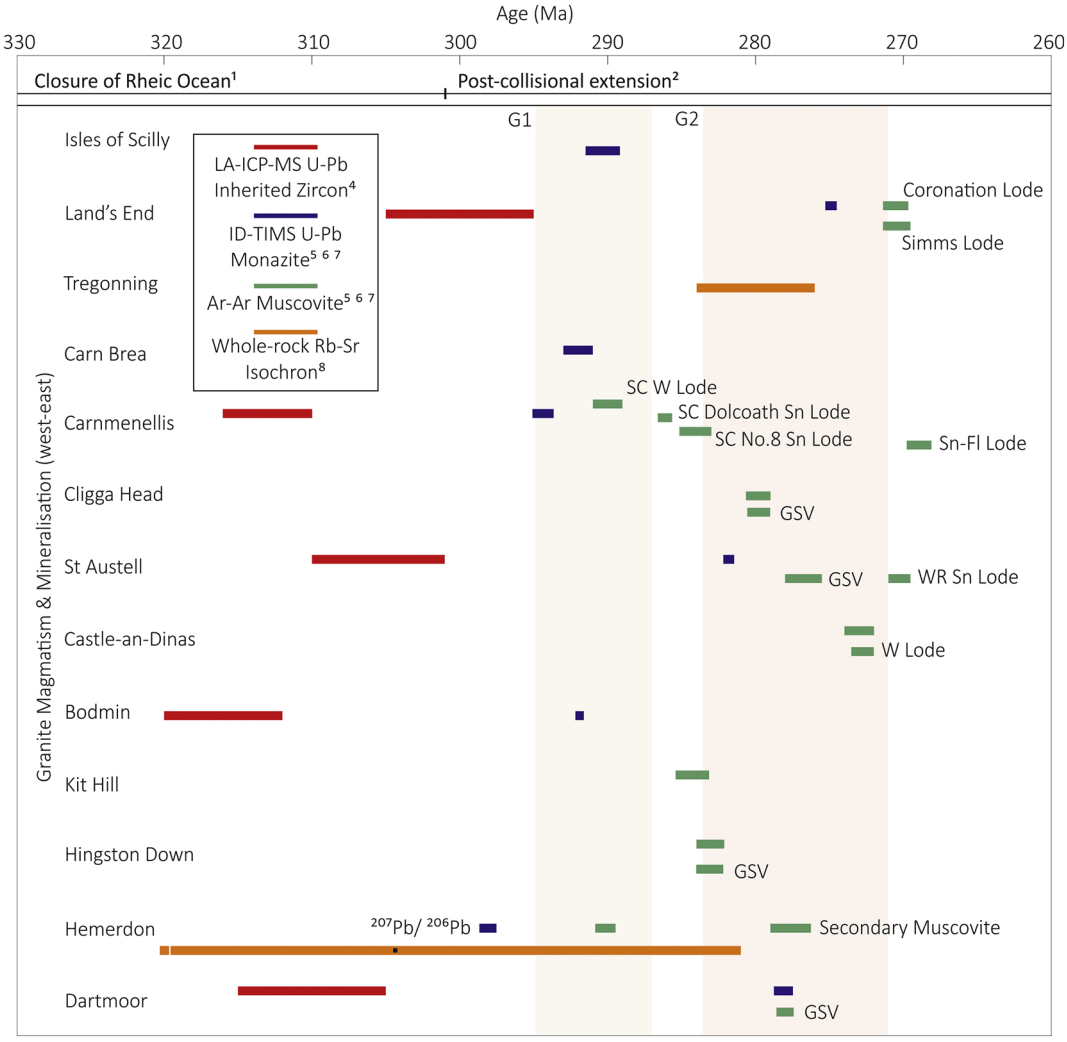
Age (Ma)
330
320
310
300
290
280
270
260
Closure of Rheic Ocean[1]
Post-collisional extension[2]
G1
G2
Isles of Scilly
Land's End
Tregonning
Carn Brea
Carnmenellis
Cligga Head
St Austell
Castle-an-Dinas
Bodmin
Kit Hill
Hingston Down
Hemerdon
Dartmoor
Granite Magmatism & Mineralisation (west-east)
LA-ICP-MS U-Pb Inherited Zircon[4]
ID-TIMS U-Pb Monazite[5 6 7]
Ar-Ar Muscovite[5 6 7]
Whole-rock Rb-Sr Isochron[8]
Coronation Lode
Simms Lode
SC W Lode
SC Dolcoath Sn Lode
SC No.8 Sn Lode
Sn-Fl Lode
GSV
GSV
WR Sn Lode
W Lode
GSV
207Pb/ 206Pb
Secondary Muscovite
GSV

Figure 2

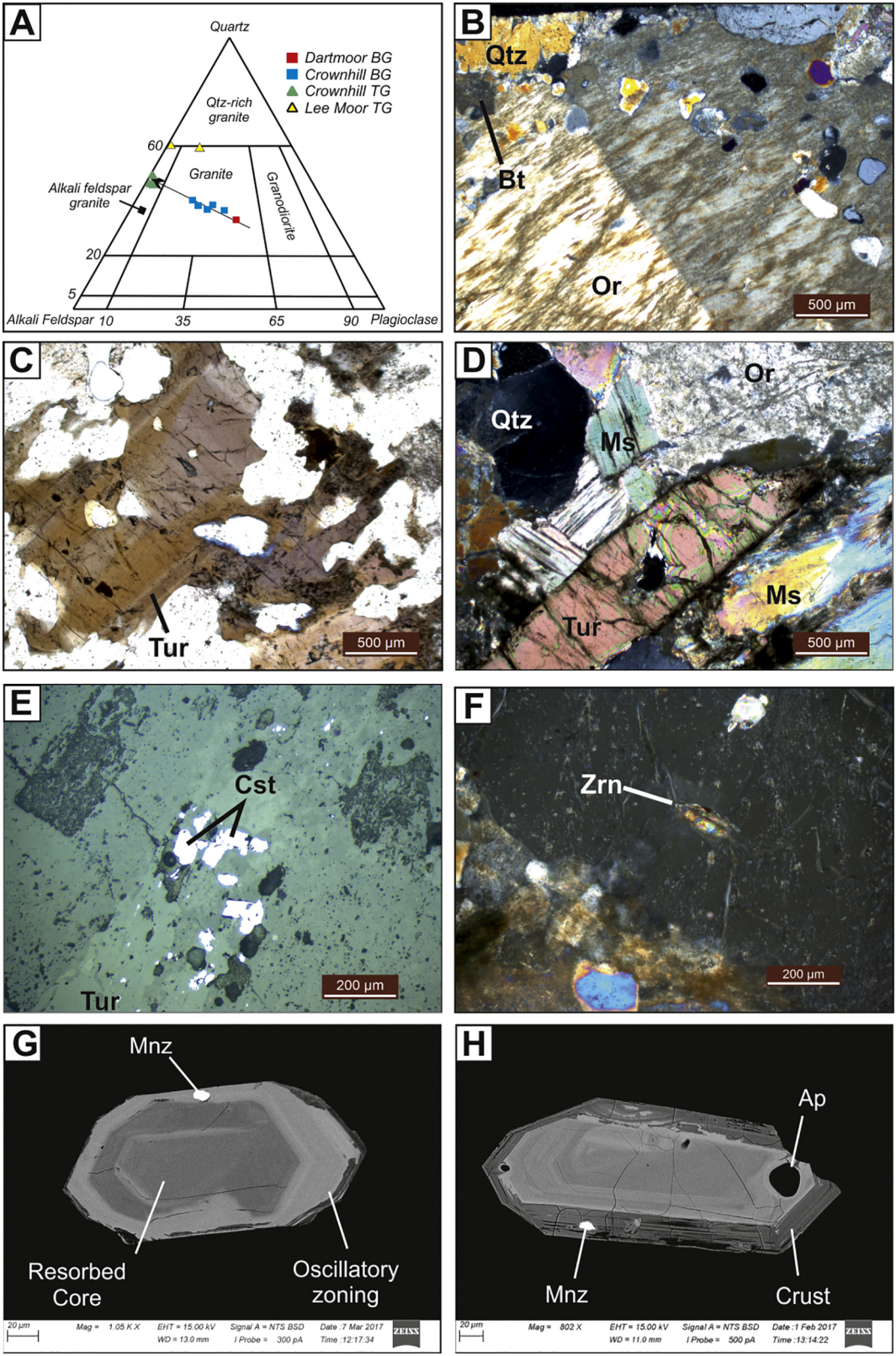
A
Quartz
Dartmoor BG
Crownhill BG
Crownhill TG
Lee Moor TG
Qtz-rich granite
60
Granite
Alkali feldspar granite
Granodiorite
20
5
Alkali Feldspar 10
35
65
90
Plagioclase
B
Qtz
Bt
Or
500 µm
C
Tur
500 µm
D
Or
Qtz
Ms
Ms
Tur
500 µm
E
Cst
Tur
200 µm
F
Zrn
200 µm
G
Mnz
Resorbed Core
Oscillatory zoning
20 µm
Mag = 1.05 K X
EHT = 15.00 kV
WD = 13.0 mm
Signal A = NTS BSD
I Probe = 300 pA
Date :7 Mar 2017
Time :12:17:34
ZEISS
H
Ap
Mnz
Crust
20 µm
Mag = 802 X
EHT = 15.00 kV
WD = 11.0 mm
Signal A = NTS BSD
I Probe = 500 pA
Date :1 Feb 2017
Time :13:14:22
ZEISS

Figure 3

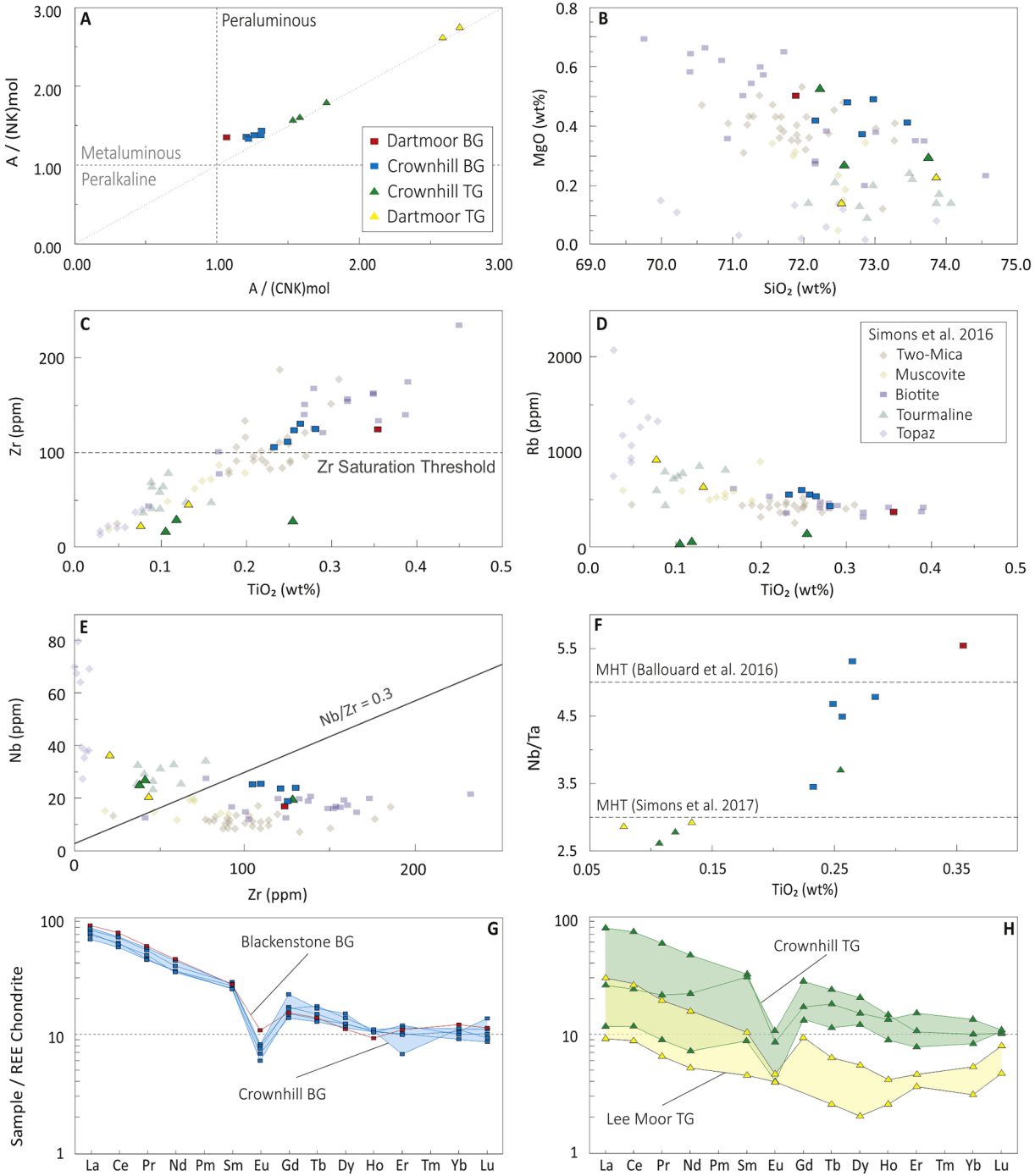
A
Peraluminous
Metaluminous
Peralkaline
Dartmoor BG
Crownhill BG
Crownhill TG
Dartmoor TG
A / (NK)mol
A / (CNK)mol
B
MgO (wt%)
SiO2 (wt%)
C
Zr Saturation Threshold
Zr (ppm)
TiO2 (wt%)
D
Simons et al. 2016
Two-Mica
Muscovite
Biotite
Tourmaline
Topaz
Rb (ppm)
TiO2 (wt%)
E
Nb/Zr = 0.3
Nb (ppm)
Zr (ppm)
F
MHT (Ballouard et al. 2016)
MHT (Simons et al. 2017)
Nb/Ta
TiO2 (wt%)
G
Blackenstone BG
Crownhill BG
Sample / REE Chondrite
La Ce Pr Nd Pm Sm Eu Gd Tb Dy Ho Er Tm Yb Lu
H
Crownhill TG
Lee Moor TG
La Ce Pr Nd Pm Sm Eu Gd Tb Dy Ho Er Tm Yb Lu

Figure 4

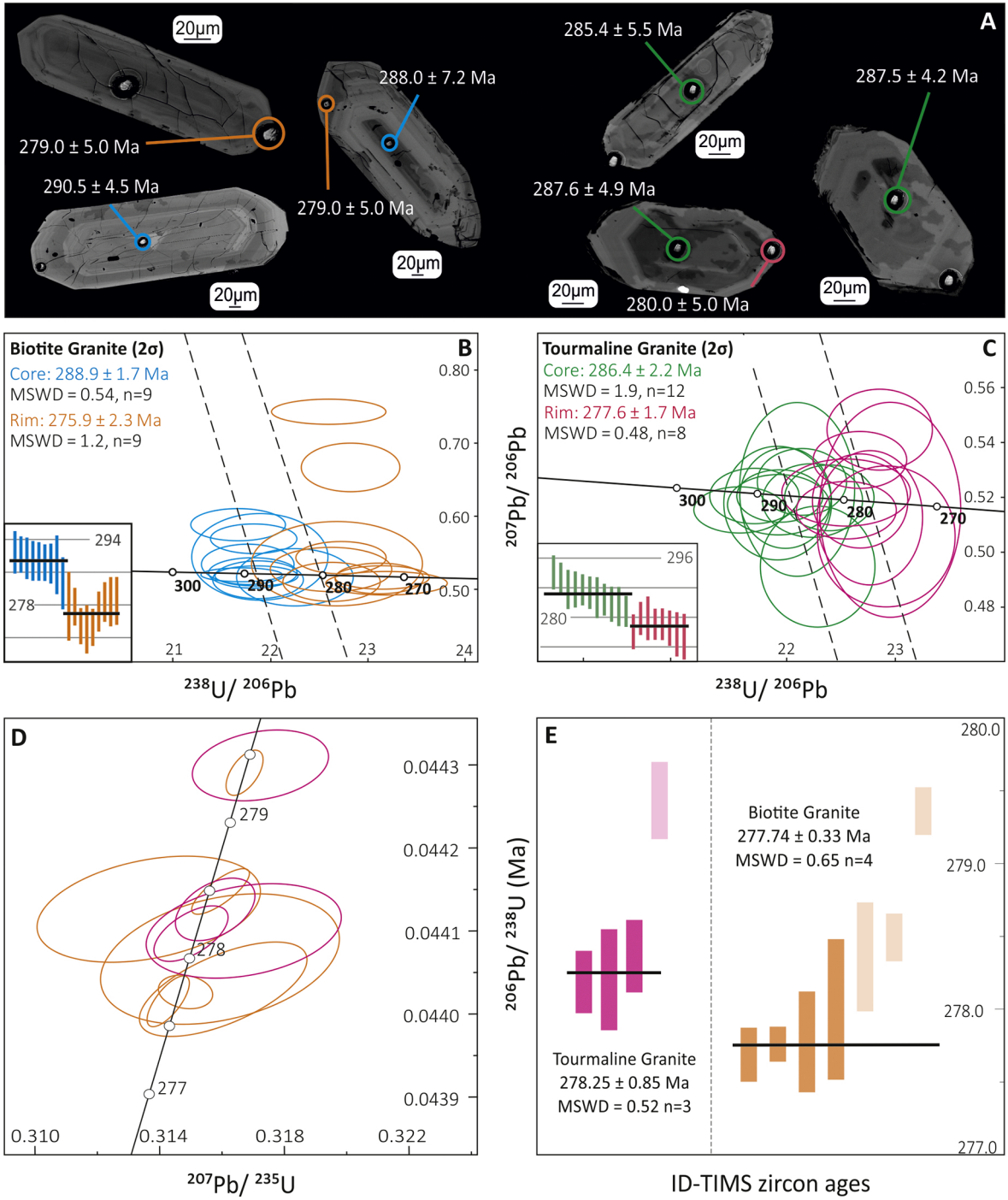
A
20μm
279.0 ± 5.0 Ma
290.5 ± 4.5 Ma
288.0 ± 7.2 Ma
279.0 ± 5.0 Ma
285.4 ± 5.5 Ma
287.6 ± 4.9 Ma
280.0 ± 5.0 Ma
287.5 ± 4.2 Ma
B
Biotite Granite (2σ)
Core: 288.9 ± 1.7 Ma
MSWD = 0.54, n=9
Rim: 275.9 ± 2.3 Ma
MSWD = 1.2, n=9
207Pb/ 206Pb
238U/ 206Pb
C
Tourmaline Granite (2σ)
Core: 286.4 ± 2.2 Ma
MSWD = 1.9, n=12
Rim: 277.6 ± 1.7 Ma
MSWD = 0.48, n=8
D
206Pb/ 238U
207Pb/ 235U
E
206Pb/ 238U (Ma)
Biotite Granite
277.74 ± 0.33 Ma
MSWD = 0.65 n=4
Tourmaline Granite
278.25 ± 0.85 Ma
MSWD = 0.52 n=3
ID-TIMS zircon ages

Figure 5

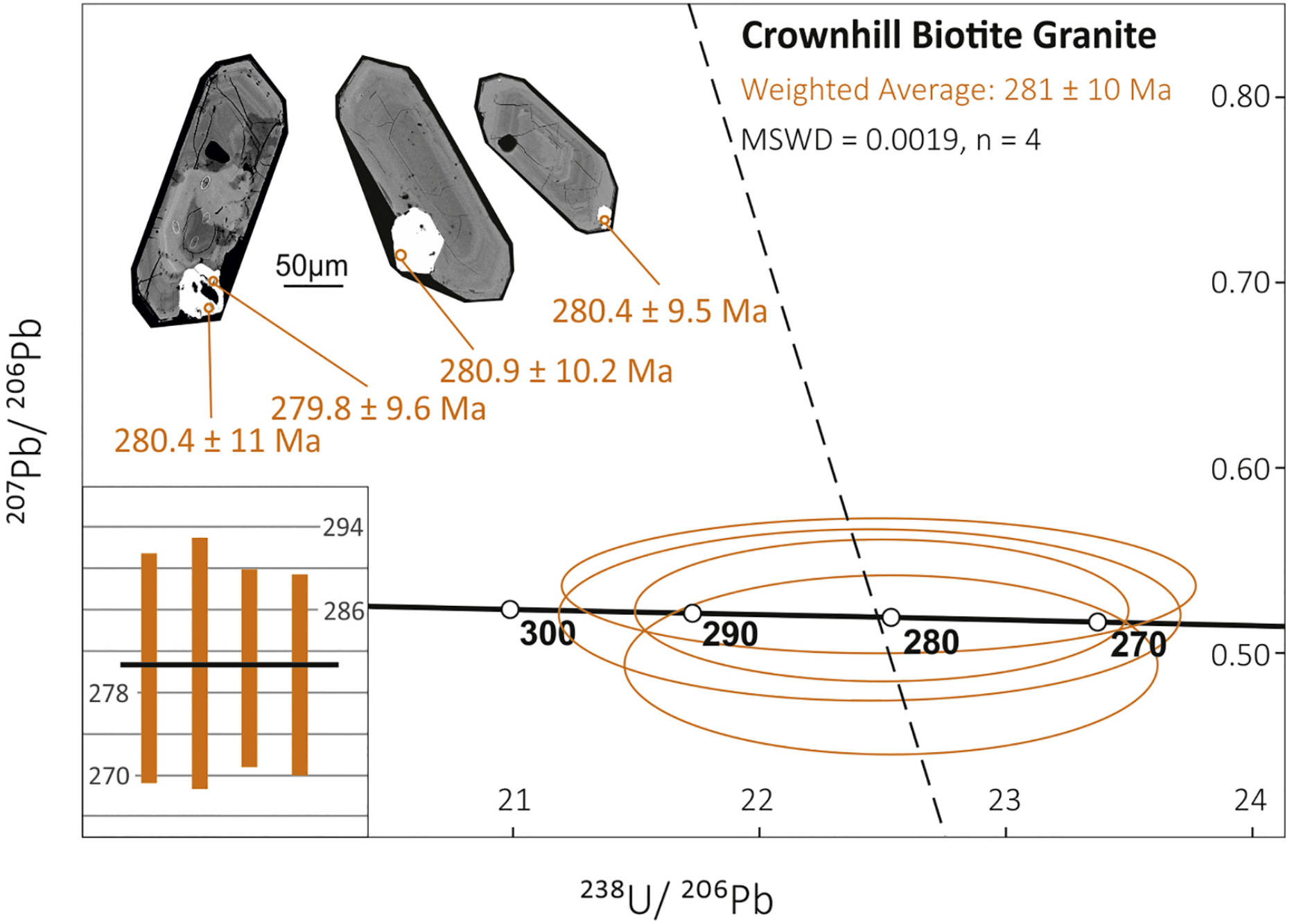
Crownhill Biotite Granite
Weighted Average: 281 ± 10 Ma
MSWD = 0.0019, n = 4
50µm
280.4 ± 9.5 Ma
280.9 ± 10.2 Ma
279.8 ± 9.6 Ma
280.4 ± 11 Ma
294
286
278
270
300
290
280
270
0.80
0.70
0.60
0.50
21
22
23
24
$^{207}Pb/^{206}Pb$
$^{238}U/^{206}Pb$

Figure 6

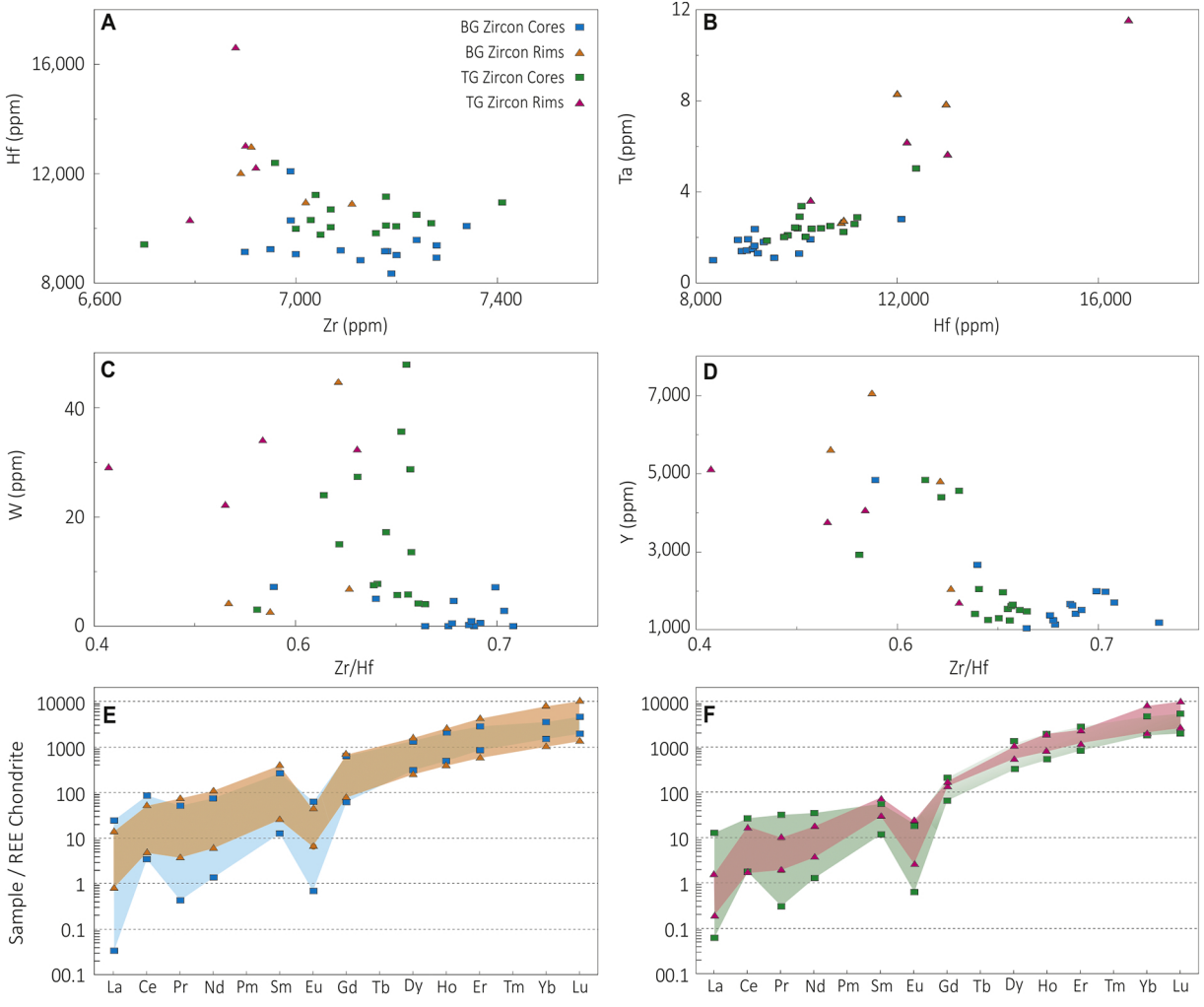
A
BG Zircon Cores
BG Zircon Rims
TG Zircon Cores
TG Zircon Rims
Hf (ppm)
16,000
12,000
8,000
6,600
7,000
7,400
Zr (ppm)
B
Ta (ppm)
12
8
4
0
8,000
12,000
16,000
Hf (ppm)
C
W (ppm)
40
20
0
0.4
0.6
0.7
Zr/Hf
D
Y (ppm)
7,000
5,000
3,000
1,000
0.4
0.6
0.7
Zr/Hf
E
Sample / REE Chondrite
10000
1000
100
10
1
0.1
00.1
La Ce Pr Nd Pm Sm Eu Gd Tb Dy Ho Er Tm Yb Lu
F
10000
1000
100
10
1
0.1
00.1
La Ce Pr Nd Pm Sm Eu Gd Tb Dy Ho Er Tm Yb Lu

Figure 7

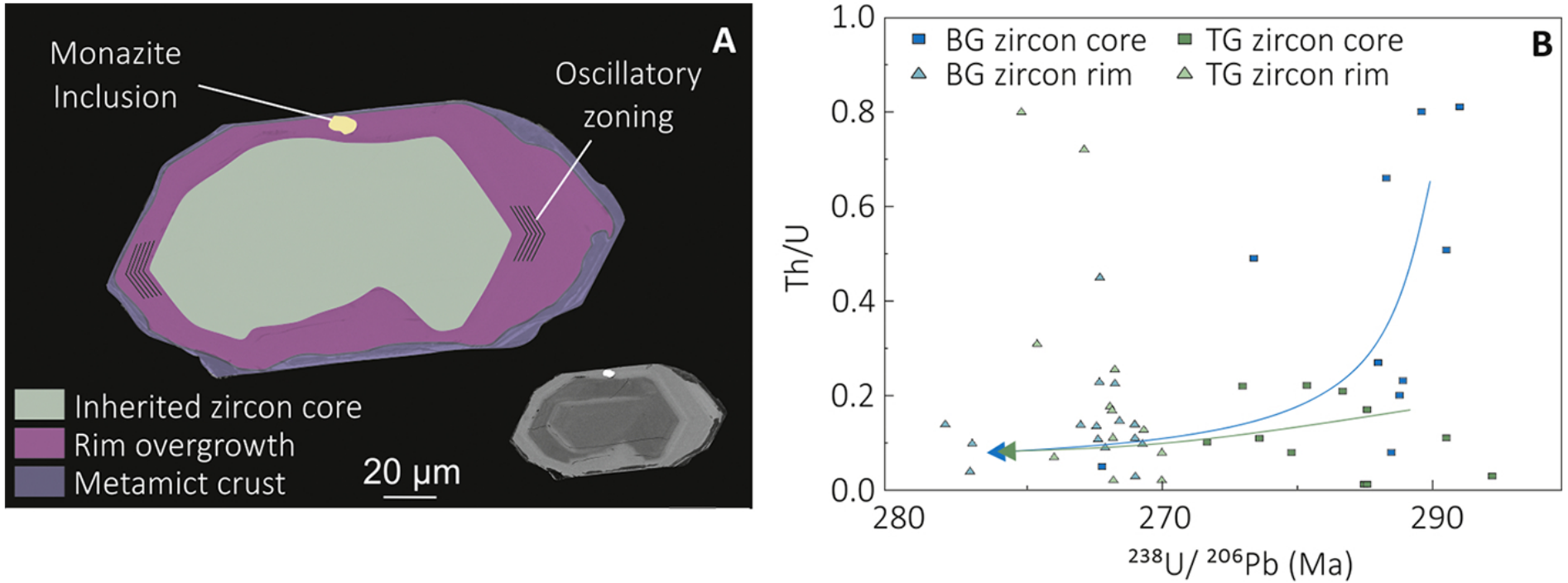
A
Monazite
Inclusion
Oscillatory
zoning
Inherited zircon core
Rim overgrowth
Metamict crust
20 μm
B
BG zircon core
BG zircon rim
TG zircon core
TG zircon rim
Th/U
1.0
0.8
0.6
0.4
0.2
0.0
280
270
290
238U/ 206Pb (Ma)

Figure 8